Automatic Detection of Concrete Surface Defects Using Pre-Trained CNN and Laser Ultrasonic Visualization Testing

Takahiro Saitoh[1], Tsuyoshi Kato[2], and Sohichi Hirose[3]

[1] *Department of Civil and Environmental Engineering, Gunma University, Kiryu, Gunma, 376-8515, Japan*
t-saitoh@gunma-u.ac.jp

[2] *Department of Informatics, Gunma University, Aramaki, Maebashi, Gunma, 371-0044, Japan*
katotsu.cs@gunma-u.ac.jp

[3] *Department of Civil and Environmental Engineering, Tokyo Institute of Technology, Ookayama, Meguro, Tokyo, 152-8550, Japan*
shirose@cv.titech.ac.jp

ABSTRACT

In recent years, nondestructive testing for civil engineering structures has become increasingly important. Ultrasonic testing is one of nondestructive inspection methods for civil structures. However, the inspection of civil engineering structures takes much time because of the extensive scope of the inspection. Moreover, in the field of nondestructive testing, there are also concerns about a future shortage of inspectors, so that an innovative effective nondestructive method needs to be developed. This study proposes an automatic defect detection approach using pre-trained convolutional neural network for laser ultrasonic visualization testing. The effectiveness of the proposed method is confirmed by applying it to a concrete structure with a surface defect. Grad-CAM demonstrates that the created CNN model in this study accurately predicts the position of a surface defect of concrete specimens.

1. INTRODUCTION

Nondestructive testing has become increasingly important for civil and mechanical engineering structures in recent years (Modarres & Keshtgar, 2016) (Helal, Sofi, & Mendis, 2015) (Rao et al., 2021). An ultrasonic method is the most widely used nondestructive evaluation method in the field (Rose, 2008) (Schmerr, 1998). The presence, absence, and location of defects in the ultrasonic nondestructive evaluation method are determined by checking scattered waves. However, it is difficult to determine the location of defects from only a simple A-scope waveform. Especially for concrete materials, this determination is more difficult because the received waveform contains a lot of noise from material inhomogeneity.

There exists a method called Laser Ultrasonic Visualization Testing [LUVT] (Takatsubo et al., 2008) that can quickly determine the existence of near-surface defects at a glance. LUVT can visualize ultrasonic wave propagation on the laser irradiated surface, as will be shown in the following section 3. The greatest advantage of LUVT and similar ultrasonic visualization techniques using laser (Köhler & Schubert, 2002) is that it can easily determine the presence and location of defects from ultrasonic visualization results, even if the inspector is not familiar with nondestructive testing. For example, (Yashiro, Toyama, Takatsubo, & Shiraishi, 2010) used LUVT to visualize ultrasonic wave propagation in welds. (Saitoh, Mori, Ooashi, & Nakahata, 2019) estimated elastic constants of CFRP [Carbon Fiber Reinforced Plastic] with the acoustic anisotropy using the image data obtained by LUVT. While LUVT has been applied to metallic and anisotropic materials like CFRP, its application to concrete has been limited. The reason for this is that ultrasonic wave propagation in concrete is extremely complicated by multiple scattering due to material inhomogeneity.

The use of artificial intelligence [AI] has attracted attention as a means of automating non-destructive inspections. AI is being considered in nondestructive testing to reduce the workload of inspectors. (Meng, Chua, Wouterson, & Ong, 2017) used a deep convolutional neural network [CNN] to identify a defect from ultrasonic waveforms. (Saitoh, Kato, & Hirose, 2021) utilized deep learning to identify the existence and type of a defect in images obtained by the time-domain boundary element method (Saitoh, Hirose, Fukui, & Ishida, 2007) that are equivalent to those obtained by LUVT. Moreover, (Han, Yang, & Liu, 2022) performed on the task of learning the

Takahiro Saitoh et al. This is an open-access article distributed under the terms of the Creative Commons Attribution 3.0 United States License, which permits unrestricted use, distribution, and reproduction in any medium, provided the original author and source are credited.
https://doi.org/10.36001/IJPHM.2024.v15i3.3855

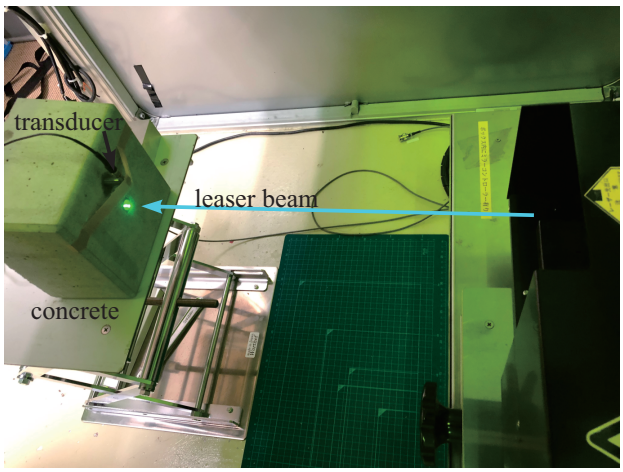

Figure 1. LUVT experimental setup for a concrete specimen.

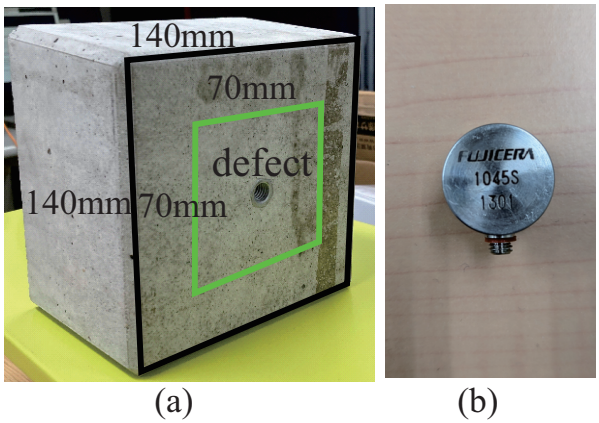

Figure 2. A concrete specimen and the AE sensor used in this study.

wave field obtained by the boundary element method to estimate the size and position of defects within the plate. Several studies have also been conducted applying deep learning to images obtained by LUVT. (Ye, Ito, & Toyama, 2018) compare the accuracy of ultrasonic propagation image classification using shallow and deep convolutional neural networks. (Nakajima, Saitoh, & Kato, 2022) predicted the existence of defects in images by performing deep CNN on image data obtained by LUVT for actual isotropic homogeneous materials. While deep learning has been applied to determine the existence of defects in LUVT images of isotropic homogeneous materials, it has not been widely used for materials with strong heterogeneity, such as concrete.

Therefore, this study aims to propose a deep learning approach to determine the existence of defects in LUVT images of concrete materials, based on previous research. In the following, we first explain the experimental conditions and other aspects of LUVT. Next, we present examples of ultrasonic wave propagation images on concrete surfaces obtained by LUVT. After a brief description of deep learning used in this study, we present the results of determining the existence of a defect in actual concrete material LUVT images. Moreover, we use the Grad-CAM to discuss which image points the AI created by deep learning pays attention to determine the existence of a defect. Finally, we summarize the conclusions and future issues.

2. LUVT SETUP

LUVT experimental conditions are introduced in this section. Fig. 1 shows the LUVT experiment setup for a concrete specimen in this research. Generally, the surface of concrete may be often rough and uneven. Therefore, the use of lasers is particularly advantageous for nondestructive testing of concrete materials. A laser emitted from the right side is irradiated onto the front surface of the concrete specimen, as shown in Fig. 1. After the ultrasonic wave excited from the laser irradiation spot propagates, a part of wave energy is received by an AE (Acoustic Emission) sensor (Skalskyi, Nazarchuk, & Stankevych, 2022). In this work, a wide band AE sensor with the nominal frequency of 200-1300 kHz is utilized as shown in Fig. 2. The surface geometry of the concrete specimen is about 140 mm $\times$ 140 mm and this concrete specimen has a penetrate cavity with diameter $\simeq$ 10 mm. This laser ultrasonic wave reception process is repeated for many irradiation spots, according to the laser scan.

Then, using the reciprocal theorem (Achenbach, 2004), the laser irradiation point and the receiving point can be swapped to obtain a waveform as if ultrasonic waves were transmitted from the receiving point. The laser irradiation points are taken within the front face of the concrete specimen, covering an area of approximately 70 mm $\times$ 70 mm, shown by the green line in Fig. 2(a). In this study, the laser pitch spacing Δx and Δy in the horizontal and vertical directions are set as $\Delta x = 0.352$ mm and $\Delta y = 0.344$ mm, respectively. The laser irradiation points N_x and N_y for each direction are $N_x = 200$ and $N_y = 196$, respectively. The distance from the laser source to the concrete specimen is approximately 500 mm. This distance, which is set sufficiently longer compared to that used in air-coupled ultrasonic testing (Chimenti, 2014), another prominent non-contact non-destructive evaluation method, offers significant advantages. The sampling rate in this measurement experiment is 12.5 MHz.

In these experimental conditions, it takes approximately 15 minutes to conduct one LUVT experiment including image data processing to obtain a set of LUVT images as mentioned in section 3. It should be noted that the time required for one LUVT experiment would increase if the defined laser irradiation area of 70 mm $\times$ 70 mm is enlarged, or if the number of laser irradiation points, N_x and N_y, is increased. Thus, due to the significant amount of time required for a single LUVT experiment and the desirability of irradiating the laser as per-

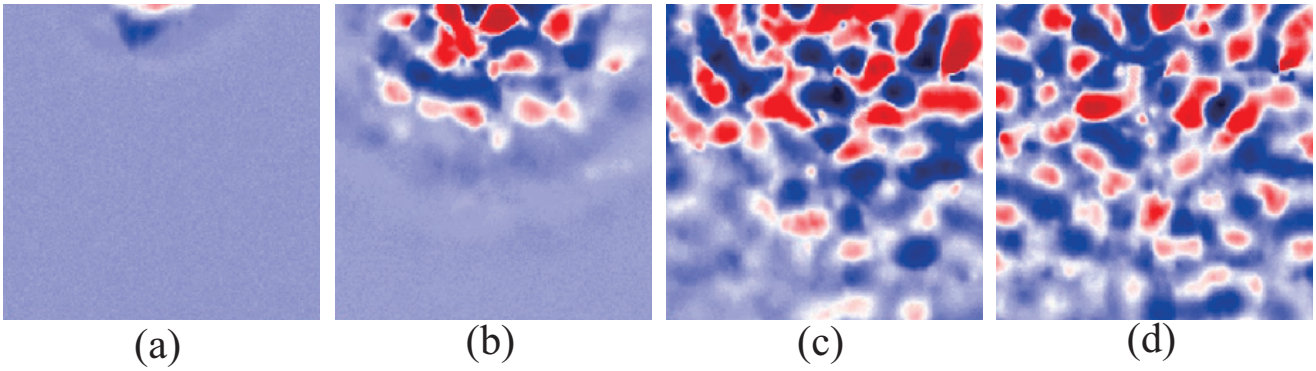

Figure 3. Time-variations of laser ultrasonic wave propagation on the surface of the concrete specimen without defect.

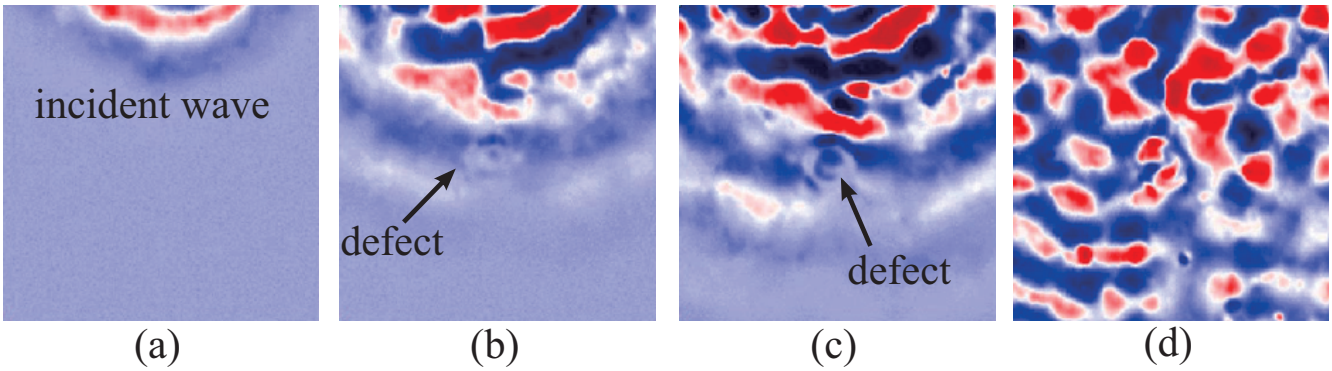

Figure 4. Time-variations of laser ultrasonic wave propagation on the surface of the concrete specimen with a defect.

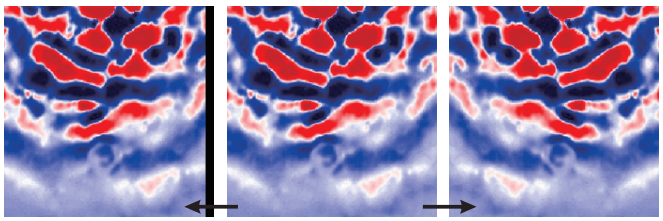

Figure 5. Example for data augmentation.

pendicularly as possible to the surface of the specimen, the parameters such as the distance from the laser source to the specimen, laser irradiation area and points have been defined as mentioned above in this study.

A number of such LUVT experiments are carried out to prepare a number of ultrasonic wave propagation images on the surface of the concrete specimen, as shown in Fig. 1. The ultrasonic wave propagation images obtained here are used as training and test data for the deep learning described in the following section 4.

3. VISUALIZATION OF ULTRASONIC WAVES ON CONCRETE SURFACE

In general, a concrete is inhomogeneous material with fine and coarse aggregates. The multiple scattering is generated by the interaction between an incident wave and the aggregates. Therefore, the incident wave with a shorter wavelength than the size of fine aggregates is not typically used due to the multiple scattering. Such wavelength limitations imply that detecting defects smaller than the aggregates is difficult. In this work, only wave components of comparable or longer wave length than general coarse aggregate size are taken into account.

Figures 3 and 4 show examples of LUVT results for concrete specimens without and with a defect, respectively. In the case with a defect, the defect is located near the center of the visualization area. In the process of image processing, a 150kHz bandpass filter is used.

As for the no defect case, the incident wave from the top center travels downward on the surface along without any defect interaction. As seen in Fig. 3, however, the ultrasonic wave propagation and scattering phenomena in concrete materials are very complicated due to the presence of aggregates.

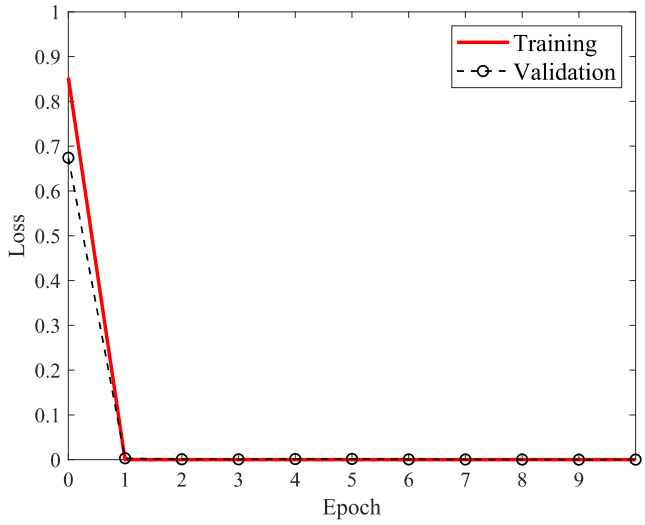

Figure 6. Relation between the epoch and training (validation) loss.

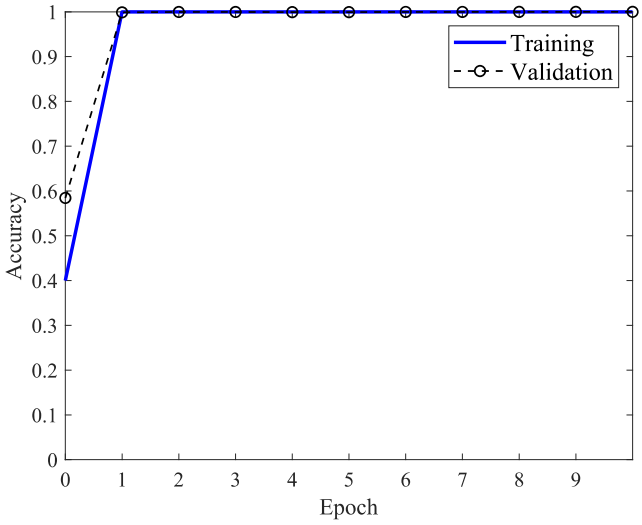

Figure 7. Relation between the epoch and training (validation) accuracy.

In the case with a defect, on the other hand, the incident wave is transmitted with multiple scattering by only aggregates at early time steps, as shown in Fig. 4 (a), where the wave behavior is not perfectly the same as those for the defect-free case as shown in Fig. 3(a), since the distributions of aggregates are different from each other. However, after the incident wave reaches the vicinity of the defect, the incident wave is disturbed by a defect as well as aggregates. In Figs. 4(b) and 4(c), it can be seen that the incident wave propagates around the cavity since it cannot penetrate inside the cavity. Then, when a certain amount of time has elapsed after the incident wave passes through the defect, as shown in Fig. 4(d), it is not possible to clearly see the presence of the defect in the LUVT image due to the repeated multiple scattering between aggregates. Note that in Fig. 4(d), ultrasonic waves seem to be seen inside the penetrated cavity because of measurement noise of LUVT.

Thus, we can obtain time sequence images of ultrasonic wave propagation in the laser irradiation area in a single LUVT test. In general, the LUVT inspector must visually determine the presence, location, and size of defects based on the images obtained from the LUVT test (or ultrasonic wave propagation movies generated from a group of images) as shown in Figs. 3 and 4. If AI can make these visual judgments, not only the workload of inspectors could be reduced, but inspections could be conducted more efficiently. Future robotic inspections will be also possible if AI can automatically determine the existence of defects. Therefore, in the following sections, we try to train a deep learning model on LUVT images as shown in Figs. 3 and 4 to classify the existence of a defect.

4. DEEP LEARNING AND RESNET50

In general, CNNs are highly effective for image-based training data. In this study, deep learning (Chollet, 2017) is applied to detect defects in images, as demonstrated in Figs. 3 and 4.

The neural network's weights are optimized through backpropagation based on the CNN's layer architecture. While users generally design their own CNN architectures, pre-built models like AlexNet (Krizhevsky, Sutskever, & Hinton, 2012) and ResNet50 (He, Zhang, Ren, & Sun, 2016) offer robust frameworks for image classification tasks. This research employs transfer learning (Pan & Yang, 2009) using the ResNet50 architecture, which is pre-trained on the extensive ImageNet dataset (Deng et al., 2009).

ResNet50 utilizes a residual network architecture to help mitigate vanishing gradients across its 50 layers, making it suitable for classifying images into 1000 categories. However, our focus is solely on binary classification to identify the presence or absence of a defect. Accordingly, the fully connected and classification layers of ResNet50 are tailored to this two-class problem.

It is noteworthy that the initial layers of a CNN typically extract general features, such as edges and contours, from images. Thus, in this study, the weights of the first 10 layers of ResNet50 are kept unchanged, while the remaining layers are retrained using the datasets illustrated in Figs. 3 and 4. For a comprehensive understanding of ResNet50's capabilities and architecture, please refer to the paper by (He et al., 2016).

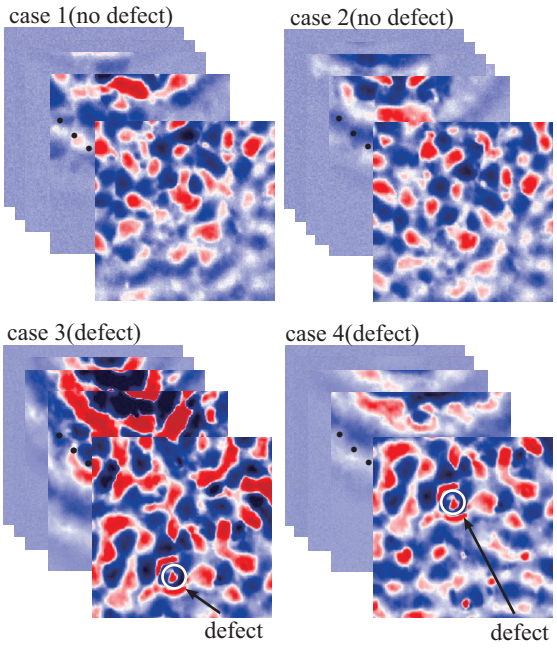

Figure 8. Test data sets for cases without a defect (case 1 and case 2) and with a defect (case 3 and case 4).

5. DEEP LEARNING RESULTS

Some deep learning results are shown in this section. The input image size is 224×224 pixels, which is aligned with the input image size used in the actual ResNet50, and the existence of a defect is determined from the output of the pre-trained CNN discussed in section 4. The stochastic gradient descent with momentum algorithm (SGDM) is used for the optimizer. The initial learning rate is 0.0003. A hold-out method is used for training, where 70 % of the total data is used for training and the remaining 30 % is used for validation. The minibatch size is 10 and the early stopping is considered for the training process. Nvidia GPU RTX 6000 with 48GB memory is utilized for CNN calculations.

5.1. Datasets and Dataset Augmentation

Deep learning is highly effective for image classification tasks but requires a substantial amount of data to achieve high accuracy. On the other hand, the implementation of the LUVT experiment as shown in Fig. 1 to obtain many training data as shown in Figs 3 and 4 requires a large amount of time. Therefore, we prepare the necessary image data for deep learning by manually performing the following data augmentation.

First, we conducted 30 different LUVT experiments for concrete specimens without a defect. Since each experiment yields a time series of 998 images, a total of 29,940 images can be obtained. However, these images include some images in which the incident wave from the ultrasonic transducer does not appear in the LUVT visualization area in Fig. 2(a). Here, we remove such images in advance. As a result, a total of 27,427 images without a defect can be prepared. Since the number of images without a defect is sufficient for training, we did not implement data augmentation for the case without a defect.

Next, we conduct 50 different LUVT experiments for the specimens with a defect. In these 50 LUVT experiments, the green laser scan area shown in Fig. 2(a) is moved up, down, left, and right randomly. As a result, the position of a defect in each set of time-history images obtained from the 50 LUVT experiments varies with each test. This means that the positions of a defect in 50 different cases are considered. On the other hand, as mentioned in section 2, the size of the defect is always constant. However, the images where the incident wave does not reach a defect sufficiently as shown in Fig. 4(a), cannot be distinguished from LUVT images without a defect. Therefore, those images are not suitable for training data for the case with a defect. Furthermore, the LUVT images such as Fig. 4(d), which are obtained when a sufficient time has elapsed after the incident wave passes through a defect, are also not adequate for the training data, since the images are greatly affected by multiple scattering from the aggregate and it may be hard to estimate the existence of a defect. Hence, among the set of images obtained in 50 LUVT experiments with a defect, only 500 images, in which the presence of a defect is clearly confirmed, such as Fig. 4(b) and (c), are selected as the training data. However, the number of images with a defect is significantly small, compared to those for the defect-free case. Therefore, by performing horizontal flipping and translation, as shown in Fig. 5, on these 500 defective images, a total of 21,000 defective images are prepared in the end.

As a result, the number of images with and without a defect are both over twenty thousand or so. Therefore, there is no significant imbalance in the number of images for each category, and the training does not adversely affect the created AI model ability to judge the presence of a defect.

5.2. Training

The results of the deep learning model developed are shown in Figs. 6 and 7. Figs. 6 and 7 illustrate the relationships between epoch and loss, and epoch and accuracy for training and validation data, respectively. The validation is performed at the end of each epoch. In both Figs. 6 and 7, the solid lines represent the results for training, while the dotted lines with circle markers represent the results for validation.

From Fig. 6, it can be observed that after the first epoch, the loss has remained at a low value for both training and validation. Conversely, as shown in Fig. 7, both training and validation have reached sufficient accuracy after just one epoch, indicating that the deep learning model has been correctly developed.

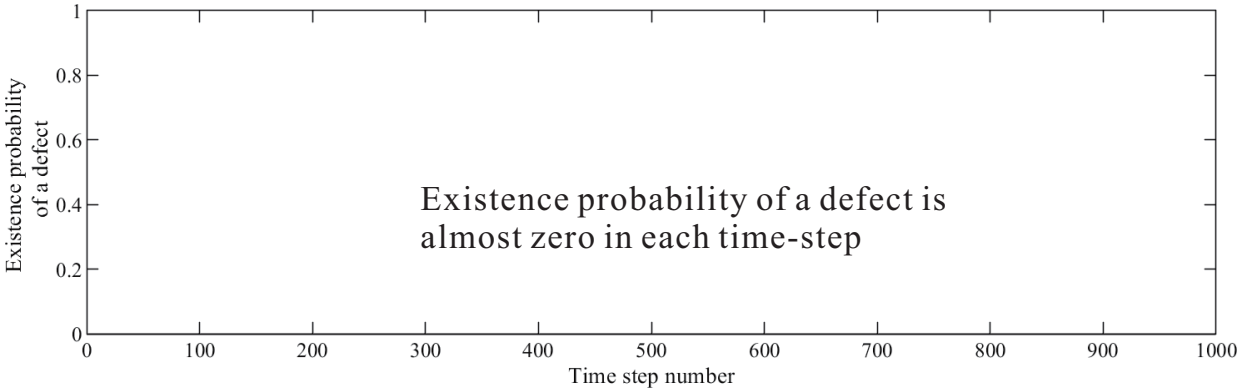

Figure 9. Surface defect detection probability for case 1 (without defect case).

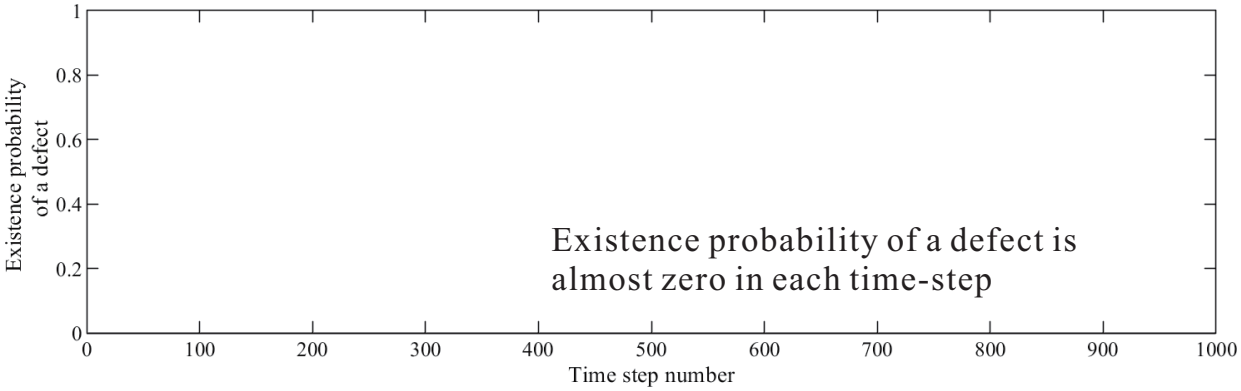

Figure 10. Surface defect detection probability for case 2 (without defect case).

5.3. Test for Unlearning LUVT Data

The AI created by using the deep learning is tested with a series of unlearning LUVT time-series image data to evaluate its ability to correctly determine the existence of a defect. As shown in Fig. 8, the test datasets of two cases without a defect (case 1 and case 2) and two cases with a defect (case 3 and case 4) are prepared. Each case consists of 998 time sequence images. In case 3, the defect is located near the lower center, while in case 4, it is positioned slightly to the upper left of the center as shown in Fig. 8.

Figures 9 and 10 show the existence probability of a defect for case 1 and case 2, respectively, which is predicted by the created AI. In each figure, the horizontal axis represents the time step number of the provided test images. As seen in Figs. 9 and 10, the existence probability of a defect shows zero for all time steps for case 1 and case 2. Therefore, it can be said that the created AI correctly predicts no defect state from the time sequence images of case 1 and case 2.

On the other hand, Figs. 11 and 12 show the existence probability of a defect for case 3 and case 4, respectively. Note that for the cases 3 and 4, the incident ultrasonic wave arrives at the defect around 250 and 300 time-steps, respectively. In both figures, we can see that the created AI shows the existence probability of a defect as zero before the incident wave reaches the defect, and the probability of defect existence sharply increases after the incident wave reaches the defect. Then, the probability of defect existence remains high for a certain period, and thereafter returns to zero with some fluctuations. The variations of detection probability with time steps reflect well the characteristics of LUVT images for the specimen with a defect as shown in Figs. 4(a)-(d). The results for cases with a defect shown in Figs. 11 and 12 exhibit noticeably different characteristics from those for cases without a defect shown in Figs. 9 and 10.

The confusion matrix for the case 1 to case 4 is shown in Table 1. From Table 1, the precision, recall, F1-score, and accuracy are 80.6%, 88.4%, 84.3%, and 95.7%, respectively. It is evident that the created model demonstrates good performance. Particularly, the high accuracy and recall indicate that the model effectively captures most of the positive class, that is, cases with a defect. However, the precision is comparatively lower. The reason is that the influence of multiple scattering makes it difficult to clearly distinguish between

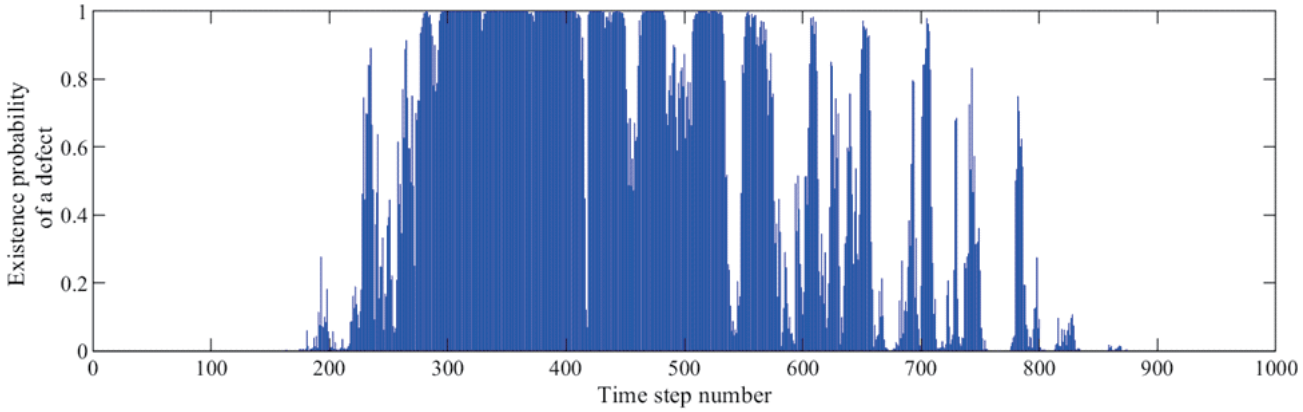

Figure 11. Surface defect detection probability for case 3 (with a defect).

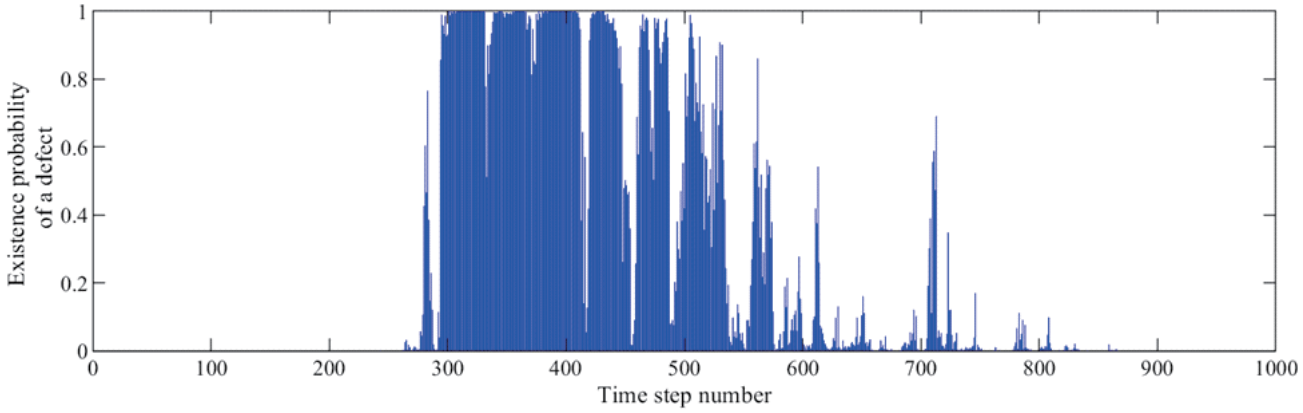

Figure 12. Surface defect detection probability for case 4 (with a defect).

Table 1. Confusion Matrix

		Predicted	
		defect	no defect
Actual	defect	466(TP)	61(FN)
	no defect	112(FP)	3353(TN)

cases with and without a defect, leading to a few uncertain classifications.

Based on the above considerations, it can be concluded that the developed AI accurately identifies the presence of a defect from the time-sequence images, even in concrete, which is an extremely heterogeneous material.

5.4. Grad-CAM

From Figs. 9-12, it can be said that the results for the unlearned images are satisfactory. However, relying solely on the black-box use of AI may lead to erroneous results. Therefore, it is desirable to confirm which part of images the created deep learning model gives attention to determine the existence of a defect. In this section, Grad-CAM (Gradient-weighted Class Activation Mapping) (Selvaraju et al., 2017) is utilized to understand which parts of images the created deep learning model focuses on to determine the existence of a defect.

In Grad-CAM, the changes for classification probabilities are calculated when slight changes are made to a portion of an image. If this classification probability change is significant, it indicates that the portion of the image where the change was made has significant impact on the classification results. Therefore, it is possible to visualize where the created deep learning model focuses in the image by displaying the magnitude of this change as a heatmap at the corresponding position in the input image. In other words, Grad-CAM is a technique used to visualize which parts of an image are focused on by a CNN when making a classification decision.

Figures 13 and 14 show the Grad-CAM results for the case 3 and case 4, respectively, which indicate where the created AI focused in each image to determine the existence of a defect. In all figures of Figs. 13 and 14, the heatmaps obtained by Grad-CAM are overlaid with the corresponding input images shown in Fig. 8. In addition, the actual defect position and size are indicated by the white circle. The time step numbers

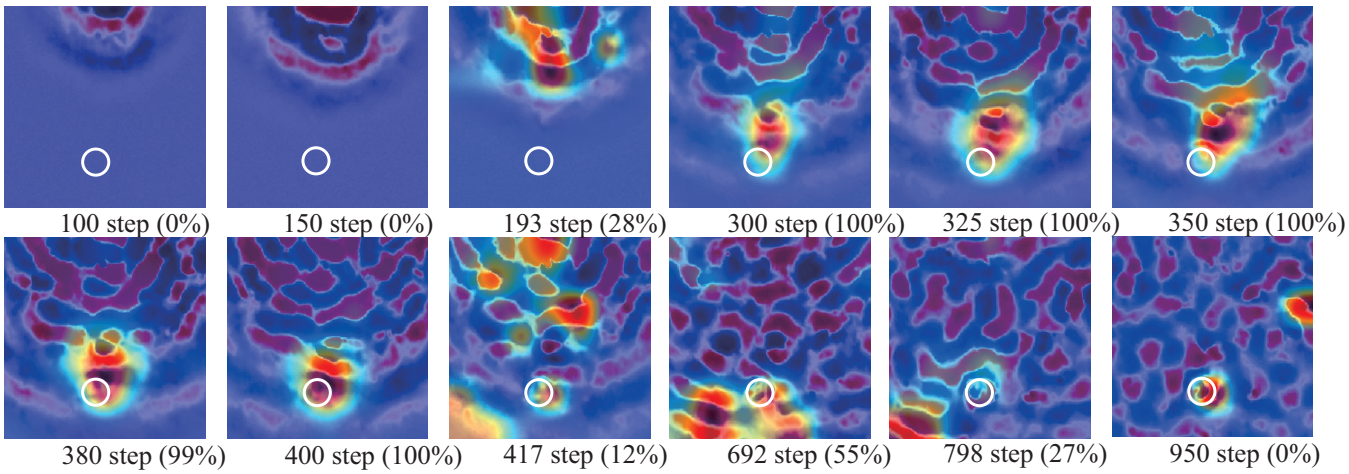

Figure 13. Grad-CAM results for various images of case 3 (with a defect).

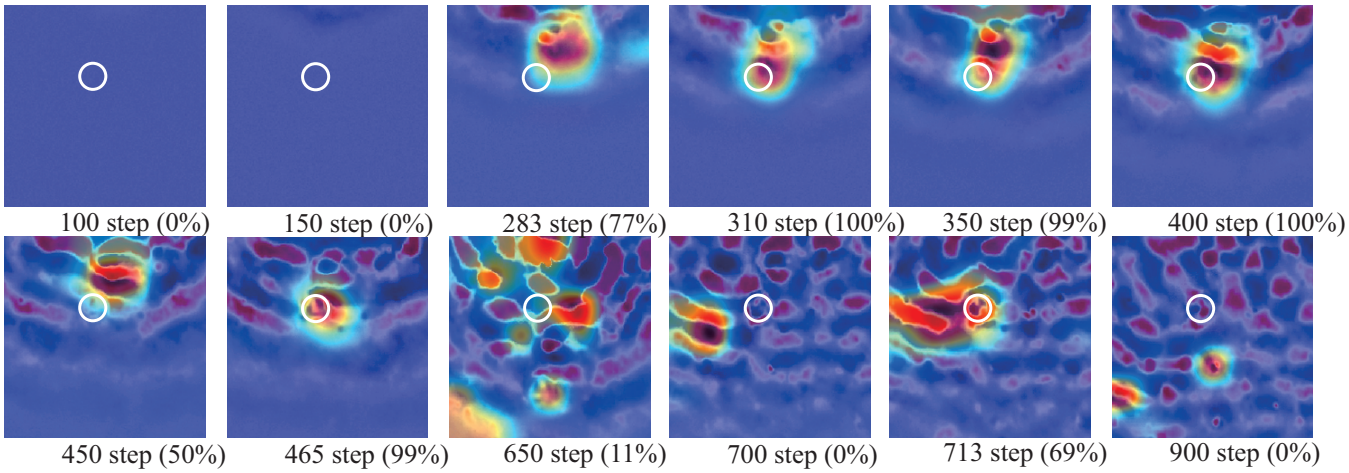

Figure 14. Grad-CAM results for various images of case (with a defect).

below each figure in Figs 13 and 14 correspond to those in Figs. 11 and 12, respectively, and the percentage indicates the existence probability of a defect.

As for the results for case 3 in Fig. 13, it can be observed that at the 100-th and 150-th time steps before the incident wave reaches the defect, the AI has not yet captured the features of the defect in the image. However, in the results for the 300-th to 400-th time steps when the incident wave reaches the defect, it can be observed that the Grad-CAM values show significant large values near the defect. On the other hand, at time steps where the probability of defect presence is low, such as 417, 798, and 950-th time-steps, it can be observed that the large values of Grad-CAM appear not only near the defect but also in other areas. Similar trends can be observed in the results presented in Fig. 14 for case 4. In case 4, the defect is positioned higher than in case 3. At 310, 350, and 400-th time-steps in Fig. 14, where the probability of defect existence is high and the existence of a defect can be correctly estimated, it can be observed that the Grad-CAM results become also large near the defect.

Thus, it can be concluded that the created deep learning model accurately tracks the defect location and determines the existence of a defect, even when the defect position changes.

Despite the advances in non-destructive testing, traditional methods like hammer sounding and contact inspections are still widely used for concrete. The LUVT implemented in this study has considerable potential to become widely used in field non-destructive teststing, especially for difficult-to-access areas, such as bridge decks and tunnels. For such industrial applications, it is essential to further develop the method pioneered in this study to inspect not only surface defects but also internal defects in concrete. Additionally, the development of robots equipped with AI like those established in this investigation might be necessary for industrial applications.

6. CONCLUSION

In this paper, we presented our approach for automatic defect detection in concrete materials using deep learning with pre-trained CNN and LUVT. In general, it is relatively easy to visually confirm the scattered waves from a defect when the target material for LUVT experiments is homogeneous like steel or aluminum (Nakajima et al., 2022). On the other hand, it can often be challenging to determine the existence of a defect from the scattered waves caused by a defect in inhomogeneous concrete materials due to the multiple scattering of ultrasonic waves by aggregates and the rapid attenuation.

In this research, we extracted only those images that clearly showed the effect of a defect and then these images were classified as containing a defect, and we conducted deep learning on them using ResNet50. Our results demonstrated that the created AI could accurately predict the existence of a defect in concrete materials. Moreover, Grad-CAM was utilized to understand which areas the AI focused on when it determined the existence of a defect.

LUVT equipment is currently very expensive. Therefore, it is difficult for it to be applied immediately in many sites. On the other hand, the practical application of research aimed at quantitatively detecting surface cracks in concrete structures using AI, based on exterior images, is advancing. LUVT, utilizing laser ultrasonics, not only allows for the inspection of concrete exteriors but also holds the potential for internal testing. Therefore, if LUVT equipment becomes more widespread and its cost of implementation decreases in the future, its industrial application may further advance.

In the future, we plan to conduct additional LUVT experiments to determine defect size and identify various types of defects. However, preparing a large number of concrete specimens, creating various artificial defects, and conducting LUVT experiments on them require significant effort and cost. To overcome the difficulty, We will explore the use of simulated image data generated using numerical methods such as the finite difference time-domain (FDTD) and finite element method (FEM), which have recently been applied by the authors with a focus on aluminum (Nakajima, Saitoh, & KATO, 2024).

Furthermore, we plan to use GAN (Goodfellow, I., Pouget-Abadie, J., Mirza, M., Xu, B., Warde-Farley, D., Ozair, S., Courville, A. and Bengio, Y., 2014) to detect a defect in LUVT images of concrete materials containing aggregates.

ACKNOWLEDGMENT

This work was supported by "Joint Usage/Research Center for Interdisciplinary Large-scale Information Infra-structures", and "High Performance Computing Infrastructure" in Japan (Project ID: jh220033 and jh230036). Additionally, funding from JSPS KAKENHI (21K0423100) and the SECOM Science and Technology Foundation supported this work.

REFERENCES

Achenbach, J. D. (2004). *Reciprocity in elastodynamics*. Cambridge University Press.

Chimenti, D. (2014). Review of air-coupled ultrasonic materials characterization. *Ultrasonics*, *54*(7), 1804-1816. doi: https://doi.org/10.1016/j.ultras.2014.02.006

Chollet, F. (2017). *Deep learning with python*. Manning Publications.

Deng, J., Socher, R., Fei-Fei, L., Dong, W., Li, K., & Li, L.-J. (2009, 06). Imagenet: A large-scale hierarchical image database. In *2009 IEEE Conference on Computer Vision and Pattern Recognition(*CVPR) (248-255). doi: 10.1109/CVPR.2009.5206848

Goodfellow, I., Pouget-Abadie, J., Mirza, M., Xu, B., Warde-Farley, D., Ozair, S., Courville, A. & Bengio, Y. (2014). Generative adversarial nets. *Advances in neural information processing systems*, 2672-2680. doi: https://doi.org/10.48550/arXiv.1406.2661

Han, X., Yang, Y., & Liu, Y. (2022). Determining the defect locations and sizes in elastic plates by using the artificial neural network and boundary element method. *Engineering Analysis with Boundary Elements*, *139*, 232-245. doi: 10.1016/j.enganabound.2022.03.030

He, K., Zhang, X., Ren, S., & Sun, J. (2016). Deep residual learning for image recognition. In *2016 IEEE Conference on Computer Vision and Pattern Recognition (*CVPR) (770-778). doi: 10.1109/CVPR.2016.90

Helal, J., Sofi, M., & Mendis, P. (2015). Non-destructive testing of concrete: A review of methods. *Special Issue Electron. J. Struct. Eng*, *14*(1), 97-105. doi: doi:10.56748/ejse.141931

Krizhevsky, A., Sutskever, I., & Hinton, G. E. (2012). Imagenet classification with deep convolutional neural networks. In F. Pereira, C. Burges, L. Bottou, & K. Weinberger (Eds.), *Advances in neural information processing systems* (Vol. 25). Curran Associates, Inc.

Köhler, B., & Schubert, F. (2002). Optical detection of elastodynamic fields of ultrasonic transducers. *Ultrasonics*, *40*(1), 741-745. doi: https://doi.org/10.1016/S0041-624X(02)00204-4

Meng, M., Chua, Y. J., Wouterson, E., & Ong, C. P. K. (2017). Ultrasonic signal classification and imaging system for composite materials via deep convolutional neural networks. *Neurocomputing*, *257*, 128-135. doi: https://doi.org/10.1016/j.neucom.2016.11.066

Modarres, M., & Keshtgar, A. (2016). Probabilistic approach for nondestructive detection of fatigue crack initiation and sizing. *International Journal of Prognostics and Health Management*, *7*, 1-10. doi: 10.36001/ijphm.2016.v7i2.2403

Nakajima, M., Saitoh, T., & Kato, T. (2022). A study on

deep cnn structures for defect detection from laser ultrasonic visualization testing images. *Artificial Intelligence and Data Science*, *3*(J2), 916-924 (in Japanese). doi: 10.1006/jabr.1994.1114

Nakajima, M., Saitoh, T., & KATO, T. (2024). Simulation-aided deep learning for laser ultrasonic visualization testing with style transfer. *Intelligence, Informatics and Infrastructure*, *5*(1), 25-33. doi: 10.11532/jsceiiai.5.1_25

Pan, S. J., & Yang, Q. Y. (2009). A survey on transfer learning. *IEEE Transactions on Knowledge and Data Engineering*, *22*, 1345–1359.

Rao, M., Yang, X., Wei, D., Chen, Y., Meng, L., & Zuo, M. (2021). Structure fatigue crack length estimation and prediction using ultrasonic wave data based on ensemble linear regression and paris's law. *International Journal of Prognostics and Health Management*, *11*. doi: 10.36001/ijphm.2020.v11i2.2923

Rose, J. L. (2008). *Ultrasonic waves in solid media*. Cambridge University Press.

Saitoh, T., Hirose, S., Fukui, T., & Ishida, T. (2007). Development of a time-domain fast multipole BEM based on the operational quadrature method in a wave propagation problem. *Advances in Boundary Element Techniques VIII*, 355-360.

Saitoh, T., Kato, T., & Hirose, S. (2021). Deep learning for scattered waves obtained by time-domain boundary element method and an attempt to classify defect types. *Journal of JSNDI*, *70*(7), 272-279 (in Japanese). doi: 10.1006/jabr.1994.1114

Saitoh, T., Mori, A., Ooashi, K., & Nakahata, K. (2019). Development of a new dynamic elastic constant estimation method for frp and its validation using the fdtd method. *Insight- Non-Destructive Testing and Condition Monitoring*, *61*(3), 162-165.

Schmerr, L. W. (1998). *Fundamentals of ultrasonic nondestructive evaluation*. Plenum Press.

Selvaraju, R. R., Cogswell, M., Das, A., Vedantam, R., Parikh, D., & Batra, D. (2017). Grad-CAM: Visual explanations from deep networks via gradient-based localization. In *2017 IEEE International Conference on Computer Vision (*ICCV) (618-626). doi: 10.1109/ICCV.2017.74

Skalskyi, V., Nazarchuk, Z., & Stankevych, O. (2022). *Acoustic emission: Fracture detection in structural materials (foundations of engineering mechanics)*. Springer.

Takatsubo, J., Miyauchi, M., Tsuda, H., Toyama, N., Urabe, K., & Wang, B. (2008). Generation laser scanning method for visualizing ultrasonic waves propagating on a 3-D object. In *1st international symposium on laser ultrasonics: Science, technology and applications.*

Yashiro, S., Toyama, N., Takatsubo, J., & Shiraishi, T. (2010). Laser-generation based imaging of ultrasonic wave propagation on welded steel plates and its application to defect detection. *Materials Transaction*, *51*(11), 2069-2075. doi: https://doi.org/10.2320/matertrans.M2010204

Ye, J., Ito, S., & Toyama, N. (2018). Computerized ultrasonic imaging inspection: From shallow to deep learning. *Sensors*, *18*(11), 3820. doi: 10.3390/s18113820

BIOGRAPHIES

T. Saitoh T. Saitoh Takahiro SAITOH is an Associate Professor at Gunma University, Japan. He received his Doctor of Engineering degree from the Department of Mechanical and Environmental Informatics at Tokyo Institute of Technology in 2006. Previously, he worked as a Japan Society for the Promotion of Science Assistant Professor at the University of Fukui, Japan. His research areas include applied mechanics, computational mechanics, and ultrasonic nondestructive evaluation. He has received several awards, including the Best Paper Award from the Japan Society for Computational Engineering Mechanics (JSCES) in 2008, the Best Paper Award from the Japan Society for Applied Mechanics (JSAM) in 2013, and the Best Paper Award from the Japan Society for Non-Destructive Inspection in 2022. He is also a member of the Japan Society for Applied Mechanics (JSAM) Committee, the Japan Society for Computational Science (JASCOME), and the Japan Society for Non-Destructive Inspection (JSNDI).

T. Kato Tsuyoshi KATO is a Professor at Gunma University, Japan. He received his Doctor of Engineering degree from Tohoku University in 2003. He is a member of JSNDI and the Information Processing Society of Japan (IPSJ). His current scientific interests include pattern recognition and nondestructive testing.

S. Hirose Sohichi HIROSE is a Professor Emeritus of Tokyo Institute of Technology, Japan. In 1987, he received his Doctor of Engineering degree from Kyoto University. He is a member of both JASCOME and JSNDI. He received several awards, including the best paper award of JSCES in 2008, the Best Paper Award from JSAM in 2013, and the Best Paper Award from JSNDI in 2022. His research interests include ultrasonic nondestructive evaluation and inverse problems.